Estimation of Cortical Bone Microstructure From Ultrasound Backscatter

Gianluca Iori, *Member, IEEE*, Juan Du, Janos Hackenbeck, Vantte Kilappa, and Kay Raum, *Member, IEEE*

***Abstract*— Multichannel pulse-echo ultrasound using linear arrays and single-channel data acquisition systems opens new perspectives for the evaluation of cortical bone. In combination with spectral backscatter analysis, it can provide quantitative information about cortical microstructural properties. We present a numerical study, based on the finite-difference time-domain method, to estimate the backscatter cross section of randomly distributed circular pores in a bone matrix. A model that predicts the backscatter coefficient using arbitrary pore diameter distributions was derived. In an *ex vivo* study on 19 human tibia bones (six males, 13 females, 83.7 ± 8.4 years), multidirectional ultrasound backscatter measurements were performed using an ultrasound scanner equipped with a 6-MHz 128-element linear array with sweep motor control. A normalized depth-dependent spectral analysis was performed to derive backscatter and attenuation coefficients. Site-matched reference values of tissue acoustic impedance *Z*, cortical thickness (Ct.Th), pore density (Ct.Po.Dn), porosity (Ct.Po), and characteristic parameters of the pore diameter (Ct.Po.Dm) distribution were obtained from 100-MHz scanning-acoustic microscopy images. Proximal femur areal bone mineral density (aBMD), stiffness *S*, and ultimate force Fu from the same donors were available from a previous study. All pore structure and material properties could be predicted using linear combinations of backscatter parameters with a median to high accuracy ($0.28 \leq$ adjusted $R^2 \leq 0.59$). The combination of cortical thickness and backscatter parameter provided similar or better prediction accuracies than aBMD. For the first time, a method for the noninvasive assessment of the pore diameter distribution in cortical bone by ultrasound is proposed. The combined assessment of cortical thickness, sound velocity, and pore size distribution in a mobile, nonionizing measurement system could have a major impact on preventing osteoporotic fractures.**

***Index Terms*— Attenuation, backscatter coefficient, cortical bone, osteoporosis, pore size, porosity, spectral analysis.**

Manuscript received August 21, 2020; accepted October 18, 2020. Date of publication October 26, 2020; date of current version March 26, 2021. This work was supported in part by the Agence nationale de la recherche and Deutsche Forschungsgemeinschaft through the TacoSound Project under Grant ANR-14-CE35-0030-01 and Grant DFG Ra1380/9-1, in part by the German Ministry of Science and Education under Grant 13GW0234, and in part by the German Ministry of Economic Affairs and Energy under Grant 03THW08H01. The work of Gianluca Iori was supported by the German Academic Exchange Service (DAAD) under Grant 91578351. The work of Vantte Kilappa was supported by the Finnish Cultural Foundation under Grant 00151113. *(Corresponding author: Kay Raum.)*

Gianluca Iori was with the Charité—Universitätsmedizin Berlin, Corporate Member of Freie Universität Berlin, Humboldt-Universität zu Berlin, and Berlin Institute of Health, Berlin Institute of Health Center for Regenerative Therapies, 13353 Berlin, Germany. He is now with the Synchrotron-light for Experimental Science and Applications in the Middle East, Allan 19252, Jordan.

Juan Du was with the Charité—Universitätsmedizin Berlin, Corporate Member of Freie Universität Berlin, Humboldt-Universität zu Berlin, and Berlin Institute of Health, Berlin Institute of Health Center for Regenerative Therapies, 13353 Berlin, Germany. She is now with Digital Endoscopy GmbH, 86316 Friedberg, Germany.

Janos Hackenbeck was with the Charité—Universitätsmedizin Berlin, Corporate Member of Freie Universität Berlin, Humboldt-Universität zu Berlin, and Berlin Institute of Health, Berlin Institute of Health Center for Regenerative Therapies, 13353 Berlin, Germany. He is now with Caresyntax GmbH, 12099 Berlin, Germany.

Vantte Kilappa was with the Charité—Universitätsmedizin Berlin, Corporate Member of Freie Universität Berlin, Humboldt-Universität zu Berlin, and Berlin Institute of Health, Berlin Institute of Health Center for Regenerative Therapies, 13353 Berlin, Germany. He is now with Mango Solutions Oy, 41120 Puuppola, Finland

Kay Raum is with the Charité—Universitätsmedizin Berlin, Corporate Member of Freie Universität Berlin, Humboldt-Universität zu Berlin, and Berlin Institute of Health, Berlin Institute of Health Center for Regenerative Therapies, 13353 Berlin, Germany (e-mail: kay.raum@charite.de).

This article has supplementary downloadable material available at https://ieeexplore.ieee.org, provided by the authors.

Digital Object Identifier 10.1109/TUFFC.2020.3033050

I. Introduction

THE mechanical integrity of cortical bone, which constitutes approximately 80% of the human skeleton mass, is a key factor of bone strength. A recent study suggested that reduced cortical thickness and the prevalence of large cortical pores in the tibia midshaft are biomarkers for reduced proximal femur strength [1]. Whereas the cortical thickness can be measured reliably *in vivo* at the central tibia shaft using second-generation high-resolution peripheral computed tomography (HR-pQCT) [2] and various ultrasound technologies, including bidirectional axial transmission [3] and refraction-corrected ultrasound imaging [4], the estimation of pore micromorphology is still challenging. Cortical porosity (Ct.Po) at the length scale of basic multicellular units (BMUs) [5] is frequently used as a surrogate biomarker for microstructural alterations in cortical bone. An increase in Ct.Po can be caused by increases in both pore diameter (Ct.Po.Dm) and pore density Ct.Po.Dn [6]. In humans, Ct.Po increases with age [7], [8], and this age dependence is more prominent in women than in men [8]. HR-pQCT is currently the only imaging modality that resolves large cortical pores *in vivo*. Several studies have shown that increased Ct.Po is associated with increased fracture risk [9], [10]. Despite these results, the imaging resolution of the first and second-generation HR-pQCT systems with voxel sizes of 82 and 61 μm allows direct visualization and segmentation of large pores (i.e., >100 μm) only, leaving the major fraction of smaller cortical pores unresolved [11], [12]. Other *in vivo* modalities, such as ultrashort

two-echo times magnetic resonance imaging (UTE-MRI) [13] and bidirectional axial transmission ultrasound (BDAT-US) [14] have been used to estimate porosity. UTE-MRI estimates a porosity index from the ratio of signal amplitudes detected from unbound and bound protons in pores and collagen matrix, respectively. A recent study of Rajapakse *et al.* [13] showed a very high *ex vivo* correlation of the porosity index with reference values of porosity ($R^2 = 0.79$) and pore size ($R^2 = 0.81$) obtained from microcomputed tomography. In an *ex vivo* BDAT-US study [15], we could predict *Ct.Po* from dispersive-guided waves with high accuracy and precision ($R^2 = 0.83$ and RMSE = 2.2 %).

It is known that biomechanical parameters, such as yield stress and elastic modulus, are inversely related to cortical pore diameter, but a positive relationship with pore density has been shown [16]. This contradictory observation can be explained by the coupled morphological changes during the development of osteoporosis. During normal bone remodeling in BMUs, osteoclasts create resorption canals, which are refilled by osteoblasts leaving a Haversian canal with a diameter in the order of 30 μm [17]. The sizes of initial resorption lacuna and remaining Haversian canal are in the range between 25 and 200 μm [16], [17], but over 60% of intracortical pores are smaller than 100 μm in diameter [12]. The shape of the pore size distribution is determined by the remodeling activity. Unbalanced remodeling leads to a transition from many small pores to fewer pores with larger diameter through delayed filling and the coalescence of BMUs [18], leaving "giant" pores with diameters larger than 385 μm [19]. The transition of existing canals toward large eroded pores is a major contributor to endocortical trabecularization and subsequent cortical thinning [20]. Therefore, detecting early deviations from a normal age- and gender-specific pore size distribution toward larger pores could indicate the onset of pathological remodeling before mechanical integrity is impaired.

High-frequency ultrasound waves have been used for decades for the characterization of soft tissues [21], [22]. Information about the size of scattering objects much smaller than the acoustic wavelength can be retrieved by spectral analysis using *a priori* assumptions about shape, material properties, and distribution of the scattering objects [23], [24]. Most established soft-tissue backscatter models are based on the scattering theory of Faran [25], which describes the scattering of sound by solid spheres and cylinders. In principle, the backscatter amplitude of a cylinder exhibits a monotonically increasing relationship with radius a, if its long axis is oriented perpendicular to the sound propagation direction and the short axis radius a is much smaller than the wavelength. Analytical solutions have been proposed for solid cylinders in fluids [25] and for fluid-saturated poroelastic cylinders embedded in a solid matrix [26]. For larger a values, the backscatter amplitude varies nonmonotonically with respect to the product of a and wavenumber k (see Fig. A-1 in the Supplementary Materials). The Faran model and the weak scattering model [27], [28] have been successfully used to describe the acoustic backscatter from cancellous bone [29], but until now, no backscatter model has been established to retrieve structural features from cortical bone. In particular, the effects of multiple scattering, mode conversion, and absorption render an analytical prediction of the backscatter coefficient for pores embedded in a solid tissue matrix difficult. A recent numerical study has used the occurrence of multiple scattering to estimate the diffusion constant D from the coherent contribution of signals backscattered from cortical pores [30]. The simulations were conducted at 8 MHz and revealed significant associations of D with both pore size and pore density. For the measurement of backscattered signals from cortical pores, the usable frequency range is further restricted. At the lower end, the acoustic pulselength must be short enough to allow a temporal separation of backscattered signals from specular reflections occurring at periosteal and endosteal bone interfaces. Thickness values at typical measurement sites in radius and tibia bones are in the range between 1 and 6 mm [3], [14], [15], [31]. The minimum pulse duration is limited by the acoustic wavelength. With the assumptions of a thickness of 1-mm and a sound velocity of 3350 m/s in the radial direction [4], the frequency must be larger than 2 MHz. At the upper end, the attenuation must be low enough to detect waves backscattered from deeper cortical bone tissue regions. Renaud *et al.* [4] suggested that a state-of-the-art ultrasound system with a dynamic range of 120 dB requires frequencies of less than 4.5 MHz to detect signals from a depth of 5-mm.

Numerical sound propagation simulations based on high-resolution images allow a detailed analysis of complex wave propagation and scatter phenomena in complex solid structures, such as cortical bone. Not only the propagation medium but also transmitter and receiver configurations and characteristics can be modeled close to real-life conditions. Previous studies have used finite-difference time-domain (FDTD) simulations based on 2-D maps derived from scanning acoustic microscopy (SAM) images with a spatial resolution of approximately 20 μm to study: 1) ultrasound transmission in the femoral neck [32]; 2) the effect of porosity on wave propagation in healthy and osteoporotic bones [33]; and 3) to estimate the effect of porosity and pore size on ultrasound multiple scattering and diffusion [30]. Most recently, 3-D FDTD models generated from the second-generation HR-pQCT data have been proposed [34].

The aims of the current study were: 1) to develop a numerical cortical bone backscatter model based on FDTD simulations and to determine the optimal frequency range for the application in human tibia cortical bones; 2) to measure acoustic attenuation and the backscatter coefficient *ex vivo* in human tibia bones; 3) to predict Ct.Po, Ct.Po.Dn, and the pore diameter distribution; and 4) to analyze their associations with mechanical properties of the proximal femur.

II. Materials and Methods

A. Human Tibia Shaft Samples

Nineteen left tibia bones from human cadavers (six male, 13 female, age: 83.7 ± 8.4 years, range: 69–94 years) described in previous studies [1], [15], [35] were used for the *ex vivo* measurements. Specimens were received without soft tissue and distal ends (cutoff at approximately 50%)

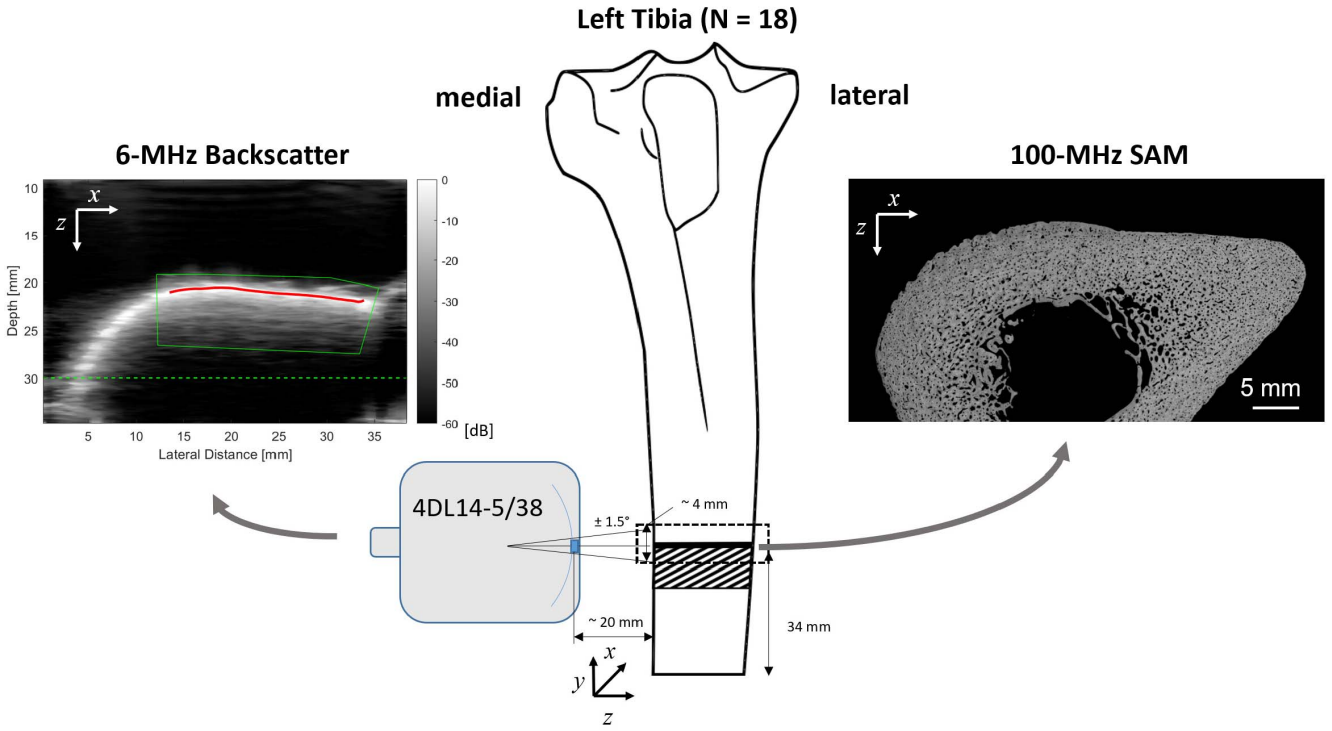

Fig. 1. Experimental workflow. At the medial side of the tibia, 6-MHz backscatter measurements were performed. The 0° sweep position of the 3-D probe was placed 34 mm above the distal cut end of the sample. The long axis of the array was positioned perpendicular to the long bone axis at an approximate distance of 20 mm. The bone surface area covered by the ±1.5° sweep scan was approximately 38 mm × 4 mm. Pulse-echo data were captured in a depth range of 35 mm. After the ultrasound backscatter measurements, 100-MHz acoustic microscopy images were obtained from site-matched cross sections. For 18 out of 19 tibia bones, a site-matched analysis could be performed.

and stored at −20 °C. The samples were collected by the Institute of Anatomy, University of Lübeck, Lübeck, Germany, in accordance with the German law "Gesetz über das Leichen-, Bestattungs- und Friedhofswesen des Landes Schleswig-Holstein II Abschnitt, §9 (Leichenöffnung, anatomisch)" from April 02, 2005. Areal bone mineral density (aBMD), macroscopic mechanical properties of the proximal femur of the same donors, has been assessed in a previous study [1]. Briefly, aBMD was measured at the femur neck using a Hologic Discovery scanner (Discovery QDR, Hologic Inc., Marlborough, MA, USA). Nonlinear homogenized voxel finite-element (hvFE) models of the proximal femur were developed from the second-generation HR-pQCT data sets [35] of the entire proximal femur to estimate stiffness (hvFE_S) and ultimate force (hvFE_Fu) under stance and side-ways fall conditions. Whereas individual hvFE models have been developed for left and right proximal femora of the 19 donors, only the properties from the left side will be compared with the corresponding left tibia properties hereinafter.

B. Cortical Bone Backscatter Measurements

A medical ultrasound scanner SonixTOUCH equipped with a SonixDAQ single-channel data acquisition system and a 3-D linear array transducer 4DL14-5/38 (Ultrasonix, Richmond, BC, Canada) was used for ultrasonic data acquisition. The SonixDAQ allows the acquisition of raw prebeamformed single-channel radio frequency (RF) data without any prior signal processing. The 128-element array-pitch element size was 0.3 mm. The sweep motor of the probe allows scanning a 3-D volume with a maximum field of view 29°. The system was controlled through a custom-developed user interface.

The schematic of the *ex-vivo* measurements is shown in Fig. 1. Measurements were performed in degassed phosphate-buffered saline (PBS) at room temperature. The medial surface of the tibia (*facies medialis*) was positioned at an approximate distance of 20 mm, such that the transducer array direction was perpendicular to the long bone axis and parallel to the bone surface. The cross-sectional imaging plane at the transducers 0°-sweep angle was approximately 34 mm away from the distal end of the sample. The bones were scanned with focused beams using a transmit aperture of 16 elements, a transmit focus of 30 mm, and an excitation frequency of 6.6 MHz, which provided a narrow unfocused beam with similar bandwidth as that used in the numerical study (Section II-E) and negligible amplitude variation in the depth range from 17 to 25 mm (as measured by means of the reflection amplitude of a planar reflector positioned at variable distances from the transducer). Scanning in the array (x) direction was achieved by translating the transmit aperture from the left to the right side of the array in 128 steps. Multidirectional beam steering was performed by both electronic beam steering ($\theta = -5°, 0°, +5°$) and array sweeping ($\phi = -1.5°, -1°, -0.5°, 0°, +0.5°, +1.0°, +1.5°$). For each transmit event, the backscattered signals were captured in a depth range from 10 to 35 mm with all 128-array elements individually at a sampling rate of 80 MHz and 10-bit resolution. The raw data (1.7 GB) were acquired within 10 s. For each tibia sample, two data sets were acquired. First, a low

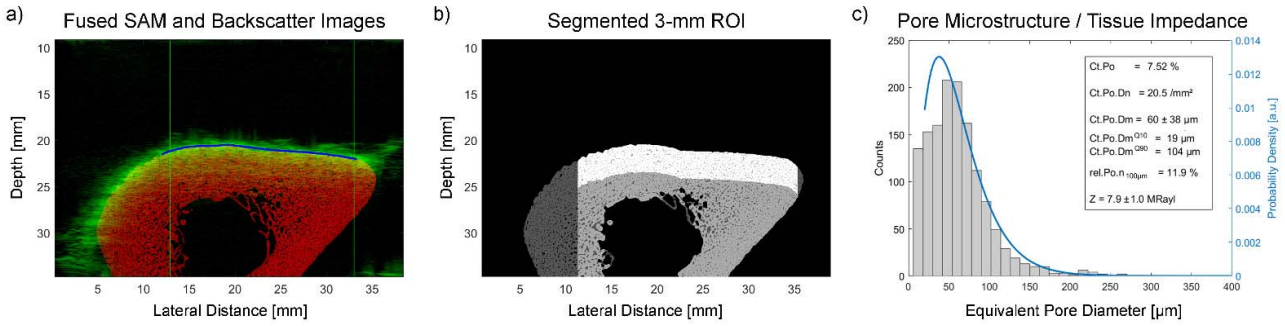

Fig. 2. (a) Spatially registered 6-MHz ultrasound backscatter (green) and 100-MHz SAM (red) images. (b) Segmented SAM image with a 3-mm stripe (relative to the periosteal bone surface) and the selected region used for the backscatter analysis marked in white. (c) Ct.Po.Dm histogram was calculated with the highlighted 3-mm ROI. From each detected pore, the equivalent diameter was calculated, a gamma probability distribution was fitted to the data, and characteristic properties of the pores and the acoustic impedance of the tissue matrix were derived.

receiver gain (35%) setting was used to ensure that no signals, particularly those reflected from the outer bone surface, were saturated. Second, a high gain (60%) was used to obtain a good signal level for the signals backscattered from the cortical bone tissue. No time-gain compensation was used for the experiments. Conventional delay-and-sum beamforming and compound imaging [36] was used to reconstruct a 3-D volume and to detect the periosteal bone surface within a manually selected region of interest (ROI) (Fig. 1).

C. 100-MHz Scanning Acoustic Microscopy

Site-matched 2-D high-resolution cross-sectional images were obtained by SAM in another study [15]. Briefly, a 2-cm-thick cross section was cut from the diaphysis using a band saw (EXACT GmbH, Remscheid, Germany) and fixed with acrylic resin (VariKleer, Buehler Ltd., Lake Bluff, IL, USA) on a sample holder. The proximal surface was polished using a grinder (Phoenix 4000, Buehler Ltd.) at a speed of 50 rpm and with decreasing grain size (ISO/FEPA grit: P80, P600, P1200, P2500, and P4000, Buehler Ltd.). Samples were then cleaned, submerged in PBS, and degassed for at least 30 min. The samples were scanned using a custom time-resolved SAM equipped with a 100-MHz focused transducer (KSI 100/60°, KSI, Herborn, Germany), which provided a lateral resolution of 19.8 μm. During the scan, the temperature was controlled and maintained at 25 °C. The scans were performed with a scan increment of 12 μm. Data were processed offline, as described in [15], to reconstruct calibrated acoustic impedance maps (Fig. 1).

D. Image Registration and Microstructure Parameter Extraction

To verify the longitudinal position of the SAM cross section, images were registered with microcomputed tomography images of the entire distal tibia shaft region [15] (data not shown). The axial positions of the SAM images were 31.9 ± 8.8 mm relative to the distal cut end. A flowchart of the individual processing steps is shown in Fig. A-2 in the Supplementary Materials. SAM and CortBS images were registered to ensure an identical selection of tissue properties [Fig. 2(a)]. The estimations of tissue impedance and structural parameters from SAM images have been described in detail in previous studies [30], [35], [37]. Briefly, the bone matrix was segmented from the background using an adaptive threshold [38]. Tissue and pore properties were analyzed within a 3-mm stripe parallel to the periosteal surface and lateral extension identical with the region selected for the backscatter analysis [i.e., the white region in Fig. 2(b) and (c)]. Ct.Po, Ct.Po.Dn, and mean acoustic impedance (Z) of the mineralized tissue matrix were extracted from the segmented pore and tissue regions, respectively. For each detected pore, the equivalent diameter was calculated. In addition to the calculation of a histogram, a Gamma probability density function was fitted to the measured pore diameter distribution

$$C(\text{Ct.Po.Dm}) = \frac{1}{b_\gamma^{a_\gamma}\,\Gamma(a_\gamma)}\text{Ct.Po.Dm}^{a_\gamma-1}e^{\frac{-\text{Ct.Po.Dm}}{b_\gamma}} \quad (1)$$

whereas C(Ct.Po.Dm) is the concentration of given pore diameter, a_γ and b_γ are shape and rate tuning parameters, and $\Gamma(a_\gamma)$ is the gamma function. The gamma distribution allows a two-parameter description of Gaussian, exponential and skewed distributions, which is widely used in life science, e.g., to describe the age-dependence of cancer incidence [39]. Mean, standard deviation, 10% and 90% quantile values, and the relative number of pores with a diameter >100 μm were extracted [Fig. 2(c)].

E. Estimation of the Backscatter Cross Section of Cortical Pores

The theoretical description of the frequency-dependent backscatter of fluid-filled elongated pores in a viscoelastic solid matrix is not as straightforward as for soft tissues [40] or for trabecular bone [41], as compression-to-shear wave conversions and multiple scattering [30] has to be considered. Therefore, a parametric numerical simulation study was performed using a 2-D FDTD code (Simsonic, Grenoble, France, http://www.simsonic.fr [42]) to derive a cortical bone-specific backscatter cross section $\gamma^{\text{mod}}(ka)$, whereas k is the wavenumber and a = Ct.Po.Dm/2. The model consisted of a 4-mm-thick cortical bone plate pervaded by randomly distributed, unisize circular pores Ct.Po.Dm (17.7, 28.5, 42.5, 55.3, 71.1, 84.0, 96.4 111.0, 126.0, and 141.0 μ m) and Ct.Po.Dn (<100 mm^{-2}), yielding Ct.Po (2%–18%, step size: 2%). The ranges of parameters were adopted from recent studies [6]–[8], [17]. The plate was positioned 4-mm below the surface

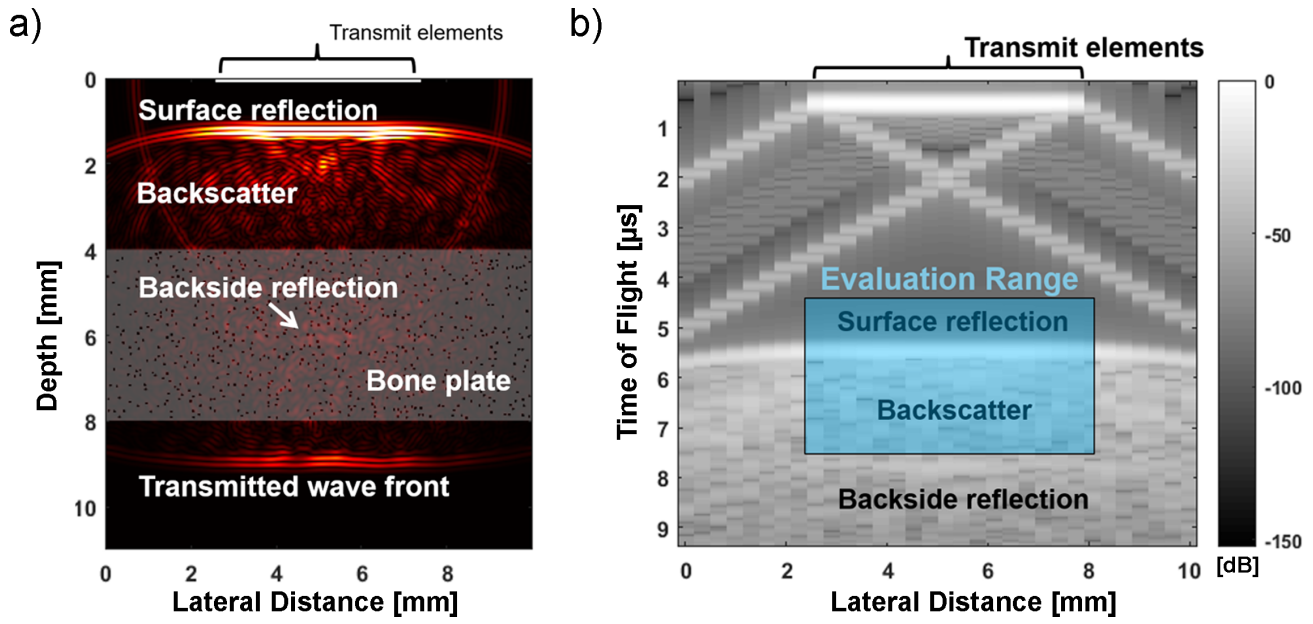

Fig. 3. (a) Snapshot of a numerical simulation model. The bone model consists of a 4-mm plate with randomly distributed pores at 4-mm distance from the transducer array. In the center, 16 transmit elements were used to emit a plane wave. Waves reflected from the bone surface, backscattered from pores, and a transmitted wavefront can be seen. Thirty-two receive elements distributed across the entire simulation field were used. (b) Pulse-echo signals (envelope) recorded by the receiver elements. Only signals recorded within the blue box, which contained the specular reflection from the surface, waves backscattered from pores, but not the waves reflected from the second bone interface, were further analyzed. Note that the excitation of the transmit element occurs at approximately 0.4 μs.

TABLE I
MATERIAL PROPERTIES USED FOR THE NUMERICAL MODEL. VALUES WERE TAKEN FROM A PREVIOUS SIMULATION STUDY [44]

	Bone	Pores
Density ρ [g/cm^3]	1.93	1.00
c_{11} [GPa]	23.7	2.25
c_{22} [GPa]	23.7	2.25
c_{12} [GPa]	9.5	2.25
c_{66} [GPa]	6.6	0
Compressional wave velocity c_p [m/s]	3500	1500
Absorption α [dB/mm]	2.1	0.002

c_{ij} are the coefficients of a transverse isotropic the stiffness tensor.

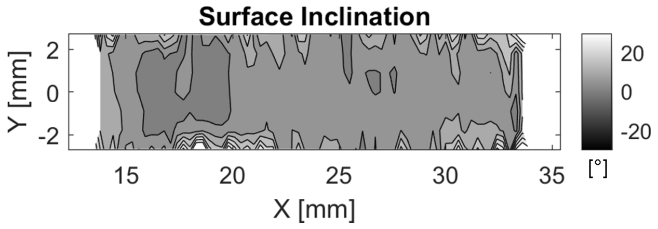

Fig. 4. Map of the periosteal surface inclination β_{ps} (in degrees) reconstructed from the backscatter data shown in Fig. 1.

of a linear array transducer with 32 elements. The size of a single element was 0.3 mm [Fig. 3(a)]. Mass density and elastic coefficients of the bone matrix and fluid are summarized in Table I. Frequency-independent absorption was incorporated in the model.

A convergence study was conducted to ensure numerical stability, as described elsewhere [43]. Stable results were obtained using a grid size of 7 μm. Sixteen central elements were used to emit a broadband 5-MHz unfocused pulse [Fig. 3(a)], whereas backscattered signals were detected with 32 receive elements. The envelopes of the received RF signals are shown in Fig. 3(b). Each bone model was generated ten times.

F. Cortical Backscatter Analysis

A flowchart of the individual processing steps is shown in Fig. A-3 in the Supplementary Materials. Conventional sum-and-delay beamforming [36] was applied to create 2-D cross-sectional beamformed images. For the experimental data, beamforming was performed for each steering and sweeping angle, and for each sweep position, the images with three steering angles were spatially compounded (Fig. 1). The time of flight of the periosteal bone surface $\mathrm{ToF}_{ps}(x, \phi, \theta)$ was detected as the locations with a maximum intensity of the beamformed compound images at each sweep angle. After appropriate scaling, local surface inclination maps $\beta_{ps}(x, y)$ were obtained (Fig. 4).

A sliding gated FFT analysis was performed using a Hanning window with a 75% overlap. Due to the different wavelengths, different window sizes were applied for numerical (0.5 μs) and experimental (0.4 μs) data. The analysis started one window length before the detected outer surface and ended about 4 mm below the surface. The result is a depth (z, relative to the bone surface, computed with the compressional sound velocity in bone assumed to be $c_p = 3500$ m/s) and frequency (f) dependent logarithmic power spectrum, which can be represented as a 6-D matrix of the form $Y(x, N_{\mathrm{Rx}}, \theta, \phi, f, z)$, where x is the center position of the transmit beam, N_{Rx} is the receive element, respectively. For each transmit event, the receive channels with prominent

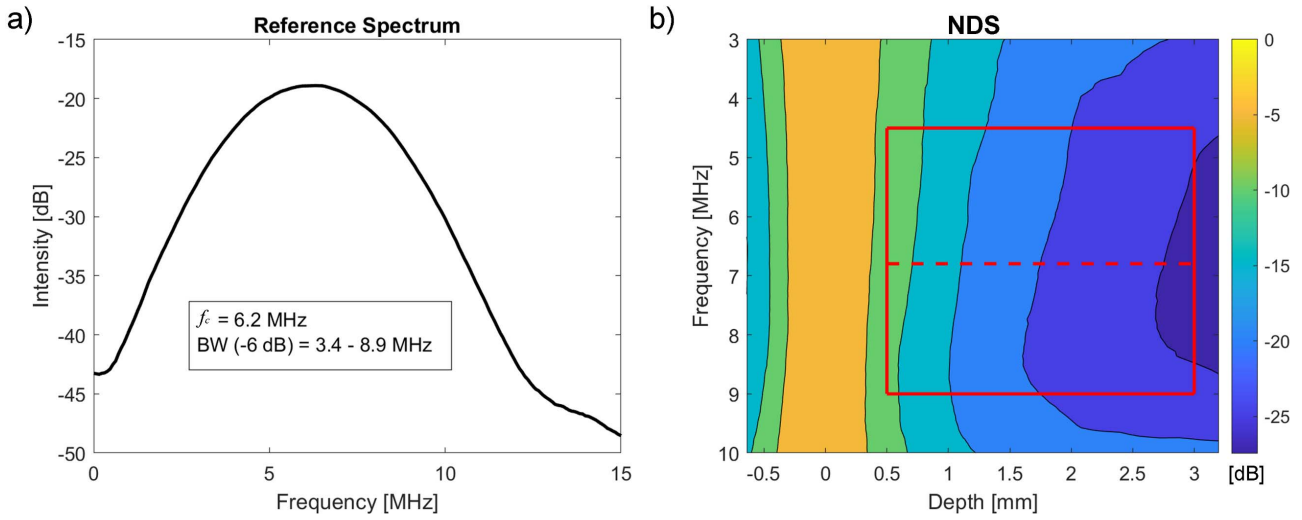

Fig. 5. (a) Reference spectrum and (b) NDS of the experimental backscatter data shown in Fig. 1.

spectral intensity (i.e., > -5 dB relative to the maximum of all channels for a given transmit event) were grouped and averaged. This resulted in a 5-D matrix of the form $Y_{\max}(x, \theta, \phi, f, z)$. For simulation data, the receive channels were averaged using receive elements between 11 and 22. The resulted spectrum is a 2-D matrix $Y_{\max}(f, z)$. Following the spectral analysis, the gate position with the highest integrated spectral intensity was estimated for each lateral transmit position (by averaging with the two adjacent locations). If the highest integrated intensity was within $\pm$ 5 gate positions of the expected surface gate, all spectra were shifted such that the maximum occurred the gate corresponding to $z = 0$. Otherwise, all spectra for this location were discarded.

The signals reflected at the periosteal surface were used as a reference for normalization. The reference spectrum represents the total reflected spectral intensity compensated for transmission losses on the propagation path. For simulation data, it was simply defined as the mean spectrum of the signals reflected from the plate front surface. For experimental data, effects arising from local surface inclinations had to be considered. Only spectra at $z = 0$, for which the local beam inclination angle was $<\pm$ 10°, were averaged [Fig. 5(a)]. For subsurface gate positions, spectra measured with a beam inclination of $>\pm$30° were removed. Moreover, any spectral value $<-$50 dB and spectra arising from the endosteal bone interface were removed. For the latter, a special algorithm searching locally for a second peak in the integrated depth-dependent backscatter was developed (data not shown). The remaining spectra were averaged within each gate position, and the reference spectrum was subtracted to obtain a normalized depth-dependent difference spectrum (NDS) NDS(f, z), as shown in Fig. 5(b). For each measurement, the peak amplitude I_{Ref} of the reference spectrum was stored.

G. Estimation Backscatter and Attenuation Coefficients

To estimate the backscatter coefficient from cortical pores, the measured backscatter spectra must be corrected for diffraction (sound field) effects and attenuation losses [23]. In this study, no diffraction correction was applied because the sound field was homogeneous within the evaluation depth range. As can be seen in Fig. 5(b), the signals decrease monotonically with increasing distance from the bone surface, but the slope inside the transducer bandwidth increases with frequency. For each frequency within the bandwidth of the transducer, the attenuated intensities measured in the depth range between 0.5–3 mm were extrapolated back to a depth of 0 mm by means of linear regression. Intercept and slope values of the regression yield the frequency-dependent backscatter and attenuation coefficients (Fig. 6).

Moreover, the upper frequency limit was dynamically adjusted, such that only frequencies up to the maximum in the attenuation coefficient were used [Fig. 6(b)]. From each measurement, the mean backscatter coefficient, slope (α_f), intercept (α_0), and attenuation values at the center frequency ($\alpha_{6-\text{MHz}}$) were derived.

For measurements in cortical bone, temporal gating, spatial sound beam pattern, and information about the probability that a pore of a certain size and form interacts with a wave within the gated tissue volume is required. The latter is typically approximated by form factors. We have approximated the theoretical backscatter coefficient (BSC) of cortical bone by

$$\text{BSC}_{\text{Ct}}^{\text{model}}(f) = G \cdot \sum_i C(\text{Ct.Po.Dm}(i)) \cdot \text{FF}_{\text{Ct.Po.Dm}(i)}(f) \cdot \gamma_{\text{Ct.Po.Dm}(i)}^{\text{model}}(f) \quad (2)$$

whereas $\gamma_{\text{Ct.Po.Dm}(i)}^{\text{mod}}(f)$ is the backscatter cross section for a certain pore diameter (Ct.Po.Dm) obtained from the numerical simulation (see Section III-B) and

$$FF_{\text{Ct.Po.Dm}(i)}(f) = e^{-12.3 f^2 \left(\frac{\text{Ct.Po.Dm}}{2}\right)^2} \quad (3)$$

is a Gaussian form factor [40], [45]. $C(\text{Ct.Po.Dm}(i))$ describes the concentration of a certain pore size within the gated volume and G is a gain factor compensating for an offset, e.g., induced by the system transfer function, the variable acoustic impedance mismatch between pore and tissue matrix, and transmission losses at the periosteal bone interface.

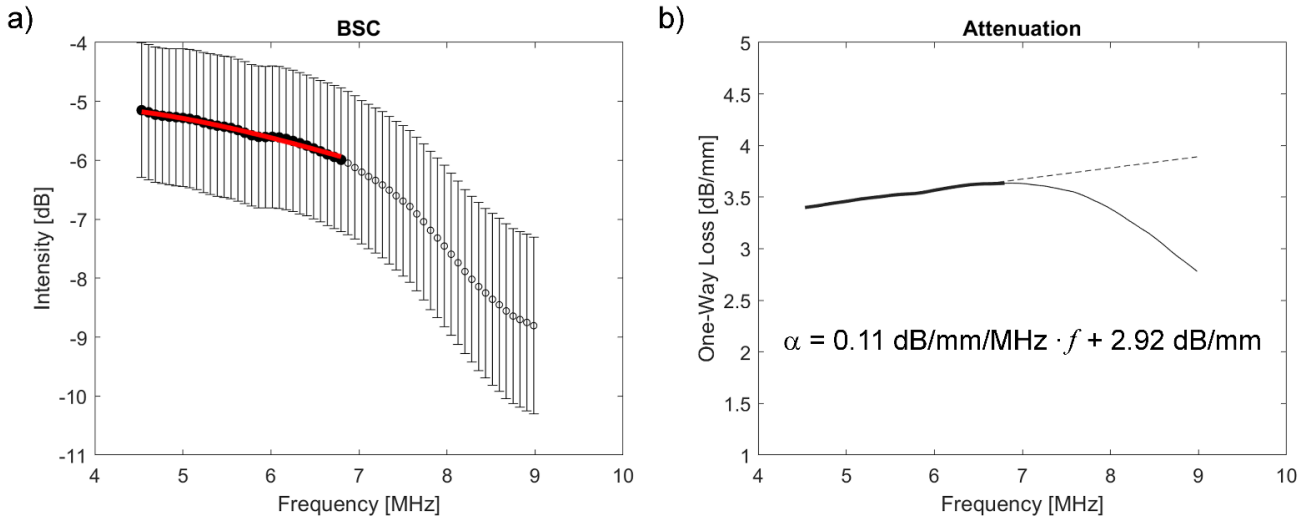

Fig. 6. (a) Measured mean and standard deviation (black) and modeled (red) backscatter and (b) attenuation coefficients derived from the two-way travel loss in the normalized depth-dependent backscatter spectrum shown in Fig. 5. Only frequency range shown with bold points and lines were used for the parameter estimations and model BSC fit.

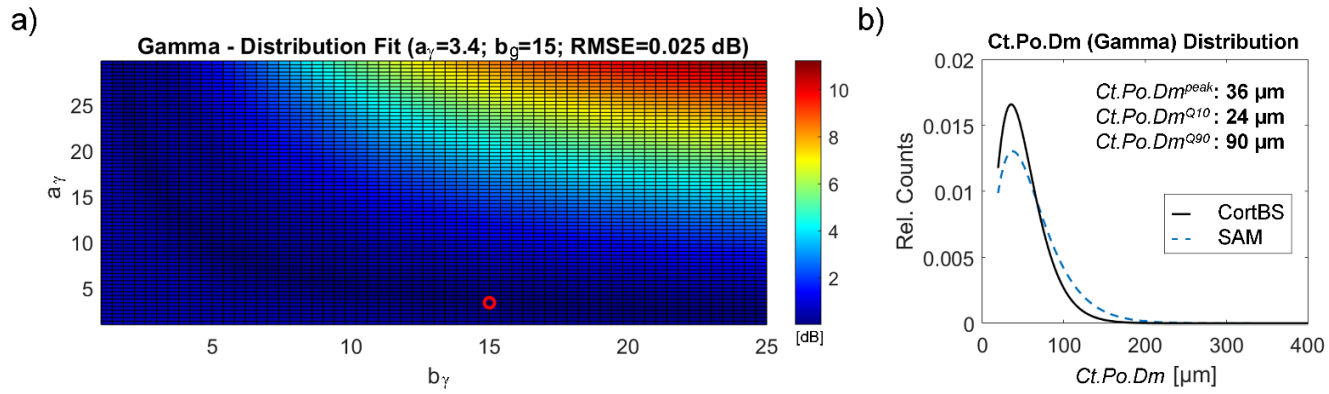

Fig. 7. (a) Plot of the error minimization for the estimation of the pore size distribution. The plot shows the RMSE between experimental and model backscatter coefficients [Fig. 6(a)]. The latter are generated using gamma-shaped pore size distributions with parameters a_γ and b_γ. The red dot indicates the minimum error, and the corresponding pore size distribution is shown in (b). The comparison of pore size distribution obtained from the backscatter measurement (CortBS) shows very good agreement with that from the SAM image [from Fig. 2(c)].

H. Estimation of the Cortical Pore Size Distribution From the Backscatter Coefficient

The pore size distribution is obtained by minimizing the difference between $\mathrm{BSC}_{\mathrm{Ct}}^{\mathrm{model}}(f)$ using an analytical pore size distribution and the measured $\mathrm{BSC}_{\mathrm{Ct}}^{\mathrm{meas}}(f)$. In analogy to the pore size analysis of the SAM images, a gamma distribution with variable tuning parameters a_γ and b_γ and an offset factor G were used for this purpose. The backscatter cross section $\gamma_{\mathrm{Ct.Po.Dm}(i)}^{\mathrm{model}}(f)$ was obtained from the numerical study (Section II-E). The error of the matching procedure and the pore size distribution that produced the best match of experimental and model coefficients [Fig. 6(a)] are shown in Fig. 7.

I. Statistics

Test for normality of the analyzed parameters was performed using a Lilliefors test. Univariate and stepwise multivariate linear regression analyses were used to evaluate the associations of backscatter properties with structural and material properties of the tibia and with mechanical properties of the proximal femur. To avoid the generation of wrong multivariate prediction models, significant models with more than two prediction variables were repeated using principal component analysis (PCA), and multivariate models are only reported if a corresponding PCA model with one or two PCA components was also significant. The accuracy of the prediction models is reported by means of adjusted R^2 and root mean squared error (RMSE) values. Statistical results were considered significant for p-values less than 0.05. All computations were performed using MATLAB (R2019b, The Mathworks Inc., Natick, MA, USA).

III. Results

One SAM image (ID1989) had to be excluded from the analysis because the bone exhibited strong signs of osteomalacia, i.e., demineralized cortical pore interfaces, leading to strong overestimations of porosity and pore size properties. In Sections III-A–III-E, only data and associations for the remaining 18 samples are reported.

A. Sample Characteristics

Areal BMD values measured in the proximal femur, cortical thickness, tissue, and pore properties obtained from the

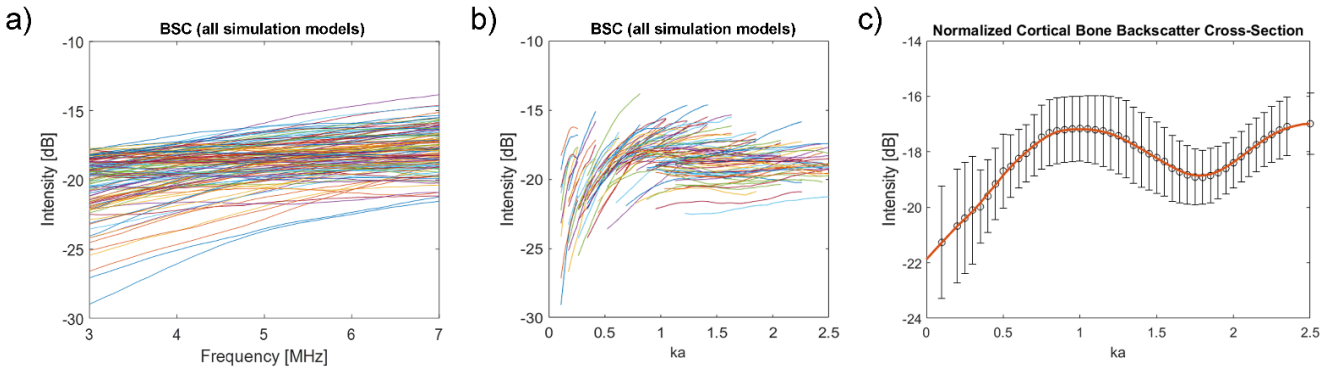

Fig. 8. (a) Attenuation corrected backscatter coefficients obtained from all numerical simulations. Each spectrum corresponds to a model with randomly distributed unisize pores of variable size and density. (b) Same data after converting f to ka. (c) Normalization to 10% porosity and averaging yields a model cortical bone backscatter cross section $\gamma^{\text{model}}_{\text{Ct.Po.Dm}(i)}(ka)$.

TABLE II
BONE PROPERTIES MEASURED WITH SAM. NOT NORMALLY DISTRIBUTED DATA ARE INDICATED BY AN ASTERISK

	MEAN ± STD	Range
aBMD [mgHA/cm²]	531 ± 98	[404 – 760]
Ct.Th [mm]	3.17 ± 1.28	[0.79 – 5.55]
Z [MRayl]	7.57 ± 0.48	[6.53 – 8.13]
Ct.Po [%]	10.7 ± 3.0	[6.3 – 17.0]
Ct.Po.Dn [mm^{-2}]	24.2 ± 4.9	[17.9 – 40.3]*
$Ct.Po.Dm^{mean}$ [µm]	61.2 ± 8.2	[36.7 – 73.6]
$Ct.Po.Dm^{peak}$ [µm]	30.4 ± 7.6	[20 – 46]
$Ct.Po.Dm^{Q10}$ [µm]	14.2 ± 1.8	[13.5 – 19.1]*
$Ct.Po.Dm^{Q90}$ [µm]	115 ± 20	[73 – 157]
$rel.Po.n_{100\mu m}$ [%]	14.0 ± 4.6	[6.8 – 23.9]

TABLE III
BACKSCATTER PROPERTIES. NOT NORMALLY DISTRIBUTED DATA ARE INDICATED BY AN ASTERISK

	MEAN ± STD	Range
I_{Ref} [dB]	-18.9 ± 1.8	[-23.3 – -17.0]*
BSC_{mean} [dB]	-5.65 ± 1.04	[-7.39 – -3.75]
α_0 [dB/mm]	2.80 ± 0.40	[2.20 – 3.52]
α_f [dB/MHz/mm]	0.14 ± 0.04	[0.06 – 0.20]
$\alpha_{6\ MHz}$ [dB/mm]	3.58 ± 0.20	[3.26 – 4.00]
Offset	-17.4 ± 2.1	[-22.3 – 14.0]
RMSE [dB]	0.042 ± 0.03	[0.01 – 0.15]*
$Ct.Po.Dm^{mean(BS)}$ [µm]	41.9 ± 17.1	[17.4 – 91.8]*
$Ct.Po.Dm^{peak(BS)}$ [µm]	34.7 ± 16.8	[20 – 88]*
$Ct.Po.Dm^{Q10(BS)}$ [µm]	27.8 ± 11.3	[20 – 68]*
$Ct.Po.Dm^{Q90(BS)}$ [µm]	70.9 ± 22.6	[40 – 118]

analysis of the tibia cross-sectional SAM images are summarized in Table II. Except for pore density and the 10% quantile pore diameter values, all properties were normally distributed.

B. Cortical Bone Backscatter Cross Section Model

Fig. 8(a) shows the backscatter coefficients obtained from the numerical study. Amplitudes and gradients varied non-monotonically with respect to pore diameter, pore density, and porosity (data not shown). On average, the backscatter intensity increased with frequency, but no clear pattern with any structural parameter change could be observed. After converting the frequency scale to a ka scale (whereas k is the wavenumber and a is the pore radius) [Fig. 8(b)] and compensating for the effect of variable porosity, a model cortical bone backscatter cross section $\gamma^{\text{model}}_{\text{Ct.Po.Dm}(i)}(ka)$ model was obtained [Fig. 8(c)].

Fig. 9 shows backscatter coefficients obtained using (2) and hypothesized pore size distributions resembling young and healthy, aged, and osteoporotic bones.

With an increasing number of large pores, the peak of the backscatter coefficient shifts toward smaller frequencies [Fig. 9(b)]. It can be seen that the change of the Ct.Po.Dm distribution from that resembling a young, healthy case to those resembling aged or osteoporotic cases is associated with characteristic changes of the BSC. Whereas the transition from young to aged cases is associated with a shift of the peak intensity of the BSC from approximately 6.4 to 5 MHz, the peak for the osteoporotic case is outside the evaluated bandwidth (<2 MHz). Thereby, the osteoporotic case exhibits generally lower backscatter amplitudes and strong negative frequency dependence. Based on these results, the frequency range between 3 and 9 MHz appears to be suitable for the evaluation of structural changes associated with aging and osteoporosis.

C. Backscatter and Pore Size Properties Obtained From 6-MHz Backscatter

Measurements taken with the low receive gain setting did prevent signal saturation from the periosteal interface. However, many signals backscattered from pores were excluded by the noise threshold. Therefore, only the measurements made with the higher gain setting were used for further analysis. Backscatter and attenuation coefficients and a corresponding pore size distribution could be obtained from all

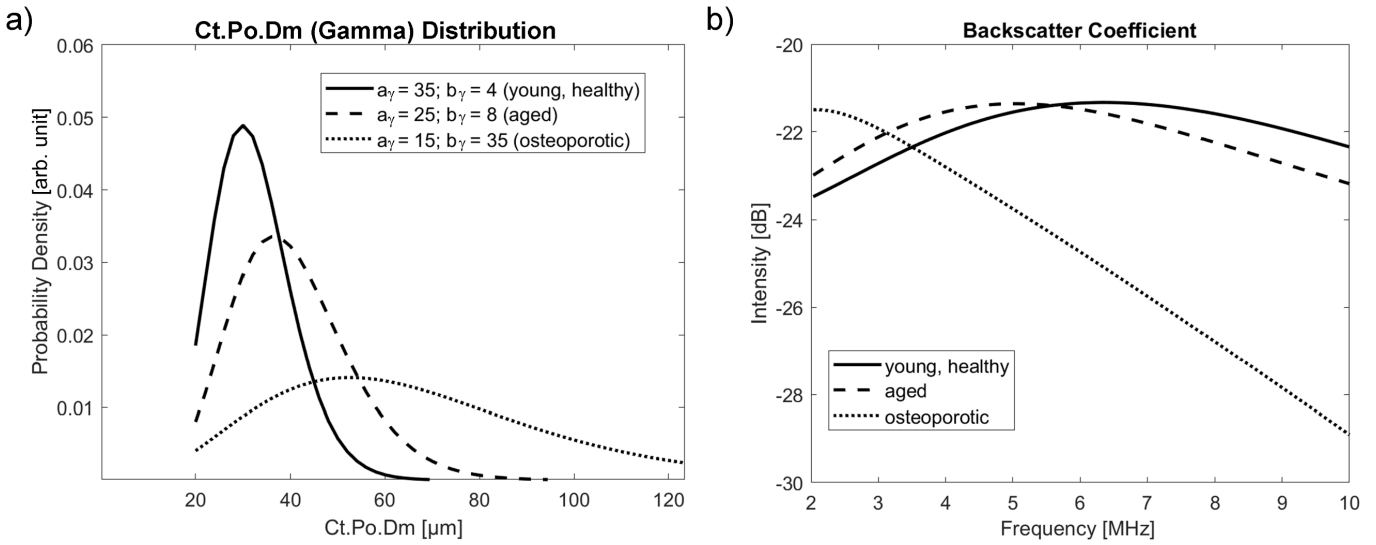

Fig. 9. (a) Representative pore diameter distributions (simulated using gamma functions with variable tuning parameters a_γ and b_γ. The distributions resemble cases typically found in young, healthy human bones, slight shifts toward larger diameters in aged humans, and the prevalence of large pores in osteoporotic cases. (b) Corresponding backscatter coefficients modeled using (2) and the cortical bone backscatter cross section $\gamma^{\text{model}}_{\text{Ct.PoDm}(i)}(ka)$ obtained from the numerical simulation [Fig. 8(b)] exhibit characteristic changes with increasing number of large pores.

samples (Table III). The mean backscatter amplitude from cortical pores was, on average, 5.6 dB lower than the amplitude of the specular reflection from the periosteal bone interface. The attenuation at the center frequency was, on average, 3.58 dB/mm, resulting in a two-way travel loss of approximately 21.5 dB for a thickness of 3 mm. The reflection from the endosteal bone interface was hardly detectable in most measurements. A very good match between measured $\text{BSC}^{\text{meas}}_{\text{Ct}}(f)$ and a model backscatter coefficient $\text{BSC}^{\text{model}}_{\text{Ct}}(f)$, derived from the model backscatter cross section $\gamma^{\text{model}}_{\text{Ct.PoDm}(i)}(ka)$ [Fig. 8(b)] and gamma-shaped pore size distribution (Fig. 7) was obtained for all measurements. The characteristic shift of the peak position in the BSC with respect to the pore size distribution, as predicted by the theoretical model, could be observed in the experimental BSCs [Fig. 9(b)]. The error between experimental and matched model BSC was very low (between and 0.01 and 0.15 dB, Table III). On average, the offset between experimental and model BSC was 17.4 dB. For the pore-size distributions derived from the backscatter measurements, the peak position values of 34.7 ± 16.8 μm were not significantly different from those obtained from the SAM images. However, the 10% and 90% quantile values were significantly larger and smaller, respectively, than their SAM-derived counterparts.

D. Associations of Cortical Backscatter Properties With Structure and Material Properties at the Tibia

Univariate linear regression results are summarized in Table A-I in the Supplementary Materials. Multivariate stepwise linear regression with up to four backscatter parameters revealed significant associations with all structure and material properties at the same measurement location (Table IV). Cortical thickness, mean, and 10% quantile values of the pore size distribution could not be predicted by any combination of backscatter parameters. The acoustic impedance of the tissue was associated (adj. $R^2 = 0.28$) with the amplitudes of the specular reflection (I_{Ref}), the mean backscatter coefficient of cortical pores (BSC_{mean}), and the slope of the attenuation coefficient (α_f). Ct.Po was highly associated (adj. $R^2 = 0.59$) with a combination of backscatter, attenuation, and predicted pore size distribution parameters. A combination of reflection, backscatter, attenuation parameters, and the 90% quantile value of the pore size distribution was able to predict pore density (adj. $R^2 = 0.46$). Reasonable to good predictions ($0.22 \leq$ adj. $R^2 \leq 0.60$) were obtained for most parameters describing the pore size distribution. In particular, the parameters describing the prevalence of large pores (Ct.Po.Dm^{Q90} and $\text{rel.Po.n}_{100\ \mu\text{m}}$, see Fig. 10) could be predicted with high accuracy (adj. $R^2 \geq 0.54$). For comparison, the last row in Table IV shows the multivariate prediction model for aBMD of the proximal femur of the same leg by backscatter properties measured at the tibia (adj. $R^2 = 0.55$).

E. Prediction of Proximal Femur Stiffness and Strength

Table V shows multivariate prediction models for proximal femur stiffness and ultimate force under stance and side-way fall conditions using: 1) tibia cortical thickness and backscatter parameters; 2) aBMD; and 3) a combination of both. For all situations except side-way fall ultimate force, Ct.Th was the single predictor and the combination with one or two backscatter parameters provided higher accuracies and lower prediction errors than aBMD. For standing loads, the best prediction model (adj. $R^2 = 0.78$) of the ultimate force was obtained by the combination of Ct.Th and aBMD.

IV. Discussion

A. Cortical Bone Backscatter Model

In this study, we have developed a theoretical model that predicts the ultrasound backscatter from pores in human cortical bone. The pores considered here are Haversian canals and remodeling cavities, which are typically elongated cylindrical structures aligned in the direction parallel to the long

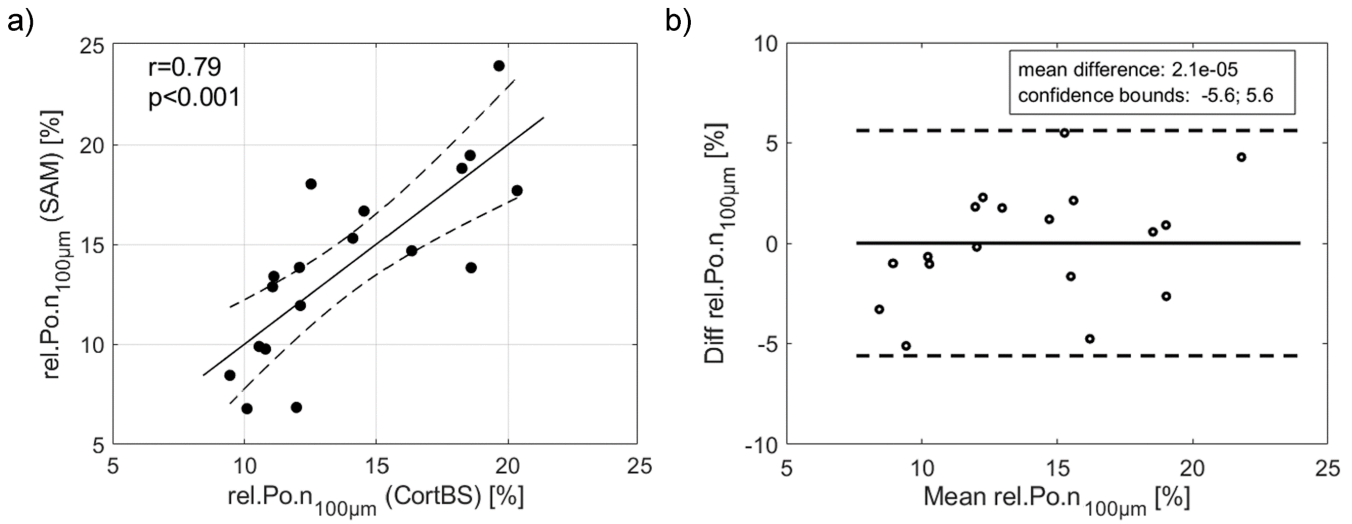

Fig. 10. Estimation of the prevalence of large pores from ultrasound backscatter parameters. (a) Linear regression between the values obtained from the multivariate linear regression model rel.Po.$n_{100\ \mu m} = f$(Offset, α_f, Ct.Po.Dm_{Q90}) and the values obtained from the SAM images. (b) Corresponding Bland–Altman plot.

TABLE IV

P-VALUES OF THE ASSOCIATIONS OF ULTRASOUND BACKSCATTER PROPERTIES AT THE TIBIA MIDSHAFT WITH SITE-MATCHED CORTICAL TISSUE AND STRUCTURE PROPERTIES OBTAINED FROM MULTIVARIATE LINEAR REGRESSION. ONLY THE P-VALUE OF SIGNIFICANT AND CLOSE TO SIGNIFICANT ASSOCIATIONS ARE SHOWN (PARENTHESIS DENOTE THAT THE SIGNIFICANCE LEVEL WAS NOT REACHED). ALL SIGNIFICANT (AND CLOSE TO SIGNIFICANT) VARIABLES WERE USED FOR THE MULTIVARIATE MODELS AND THE CORRESPONDING R^2, P, AND RMSE VALUES ARE SUMMARIZED IN THE LAST THREE COLUMNS. THE LAST ROW SHOWS THE ASSOCIATION WITH aBMD MEASURED AT THE PROXIMAL FEMUR OF THE SAME LEG

	BSC_{mean}	Offset	α_0	α_f	α_{6MHz}	I_{Ref}	*Ct.Po.Dm*			Adj. R^2	*p*-value	RMSE
							Peak	*Q10*	*Q90*			
Tibia Properties												
Ct.Th											n.s.	
Z	(0.06)			0.01		0.01				0.28	0.05	0.41 MRayl
Ct.Po	0.03	0.009		0.008				0.02	0.01	0.59	0.005	1.95 %
Ct.Po.Dn	0.02				0.02	0.03			0.01	0.46	0.01	3.58 mm^{-2}
Ct.Po.Dm^{mean}											n.s.	
Ct.Po.Dm^{median}									0.03	0.22	0.03	8.3 µm
Ct.Po.Dm^{peak}				0.002						0.41	0.002	5.8 µm
Ct.Po.Dm^{Q10}											n.s.	
Ct.Po.Dm^{Q90}		0.006		0.04				0.02	0.001	0.60	0.002	12.9 µm
rel.Po.$n_{100\mu m}$		0.005		0.002					0.001	0.54	0.003	3.1 %
DXA												
aBMD	0.002			0.005	0.01	0.003	0.004	0.01	0.02	0.55	0.02	66 mgHA/cm²

bone axis [11]. The model is based on the backscatter cross section $\gamma^{\text{model}}_{\text{Ct.Po.Dm}(i)}(ka)$ of randomly distributed unisize cylindrical pores embedded in a solid matrix. $\gamma^{\text{model}}_{\text{Ct.Po.Dm}(i)}(ka)$ was derived using 2-D-FDTD simulations, which allowed the incorporation of realistic structure and material properties of human cortical bone. The elastic simulation model considers frequency-dependent scattering, multiple scattering, wave conversions, and frequency-independent absorption losses. As the simulations were performed in 2-D, assuming the cylindrical pores oriented normal to the image plane, the model is only valid for the case that the sound propagation direction is approximately perpendicular to the long axis of the pores. To account for the heterogenous distribution of pore diameters typically found in human bone [Fig. 2(c)], the size distribution was approximated by a gamma distribution, and the backscatter coefficient was estimated as a weighted sum of backscatter from all pores using a form factor model [40]. This model predicts that changes in the pore diameter distribution

TABLE V
ASSOCIATION OF PROXIMAL FEMUR STIFFNESS AND ULTIMATE FORCE WITH TIBIA ULTRASOUND BACKSCATTER PARAMETERS AND CORTICAL THICKNESS. FOR COMPARISON, THE ASSOCIATIONS WITH aBMD MEASURED AT THE PROXIMAL FEMUR AND SIGNIFICANT SINGLE PARAMETER REGRESSIONS ARE ALSO PROVIDED IN DESCENDING ORDER OF PREDICTION ACCURACY

	Model	Adj. R^2 (p)	RMSE
FE (STANCE)			
hvFE_S	$= f(Ct.Th, Ct.Po.Dm_{Q10})$	0.65 (0.0001)	776 N/mm
	$= f(Ct.Th)$	0.58 (0.0001)	845 N/mm
	$= f(aBMD)$	0.35 (0.005)	1056 N/mm
	$= f(a_\beta)$	0.20 (0.04)	1176 N/mm
hvFE_Fu	$= f(Ct.Th)$	0.69 (<0.0001)	487 N
	$= f(Ct.Th, aBMD)$	0.78 (<0.0001)	412 N
	$= f(aBMD)$	0.55 (0.0003)	590 N
FE (FALL)			
hvFE_S	$= f(Ct.Th, BSC_{mean}, \alpha_\beta, Ct.Po.Dm_{Q90})$	0.52 (0.009)	267 N/mm
	$= f(aBMD)$	0.40 (0.003)	298 N/mm
	$= f(Ct.Th)$	0.21 (0.03)	342 N/mm
hvFE_Fu	$= f(Ct.Th, Offset)$	0.451 (0.005)	349 N
	$= f(aBMD)$	0.58 (0.0001)	305 N
	$= f(CtTh)$	0.37 (0.004)	372 N

during normal aging or the onset of osteoporosis [17] results in changes in mean amplitude, peak position, and frequency dependence of the backscatter coefficient in the frequency range between 2 and 10 MHz (Fig. 9). Most importantly, a gradual transition of the peak in the BSC from approximately 6.4 to < 2 MHz occurs for pore size distributions resembling healthy, aged, and osteoporotic cases were predicted by the model, suggesting that this frequency range is suitable for the assessment of microstructural changes *in vivo*. The inverse approach, i.e., the prediction of the pore size distribution from a measured backscatter coefficient, was applied *ex vivo* on 18 human tibia bones using a medical ultrasound scanner equipped with a 128-channel data capture system and a 3-D-linear array probe. The developed data acquisition and analysis enabeled multidirectional scans, provided image guidance, and thereby proper positioning of the probe relative to the bone surface, a precise estimation of the beam inclination for every scan position, and an automatic calibration of the backscatter spectra measured in cortical pores based on the specular reflection from the periosteal bone surface. Within the used frequency range, the normalized depth-dependent spectrum provided good separation of specular reflections from waves backscattered from cortical pores and allowed an attenuation-compensated analysis of backscatter and attenuation coefficients in a depth range from 0.5 to 3 mm. To the best of our knowledge, this is the first report on the experimental assessment of the BSC in cortical bone. The backscatter amplitudes were approximately 5.6 dB lower than the amplitudes of the specular reflection from the bone surface and exhibited a strong attenuation of up to 4 dB/mm at 6 MHz. Attenuation in cortical bone, particularly the derived attenuation coefficient, depends strongly not only on the ultrasound frequency [46] but also on the tissue type, propagation direction, and porosity [47]. Reported attenuation values for cortical bone are lower in the longitudinal bone direction than in the radial and tangential directions and are lower in plexiform tissue than in Haversian tissue [47]. For the latter, attenuation increases with increasing porosity. Sasso *et al.* [47] measured attenuation coefficients of 5.4 and 9.9 dB/MHz/cm at 4 MHz in the radial direction of bovine bones composed of Haversian bone (pore size between 20 and 50 μm) and porous bone (pore size between 50 and 300 μm), respectively. These values correspond to absolute attenuation values of 3.2 and 5.9 dB/mm at 6 MHz for normal Haversian and porous bones, which is equivalent to the range of 3.26–4.00 dB/mm, which was measured at 6 MHz in this study.

Because of the high attenuation loss and the limited dynamic range of the system, the measurements made with a high receiver gain had to be used. On the one hand, these settings led to digital saturation of signals reflected from the bone surface, which was at least in part corrected by the bandpass filters applied to the signals prior to the spectral analysis. On the other hand, the analysis could be performed for all samples in the entire 3-mm depth range, and signals reflected from the endosteal interface were mostly not apparent. The derived attenuation coefficients exhibited an expected positive slope for low frequencies, but in most cases, decreased at higher frequencies [Fig. 6(b)], which was caused by the

limited dynamic range. Despite the limited usable bandwidth, a unique model backscatter coefficient could be matched to each measurement [Figs. 6(a) and 7(a)], leading to a pore size distribution estimation [Fig. 7(b)]. Although the peak positions in the pore diameter distributions obtained from the cortical backscatter measurement were not significantly different from those obtained from the SAM images, the individual parameters derived from the pore diameter distributions were not directly correlated. This is not unreasonable for the following reasons: 1) the reference values were derived from 2-D SAM-sections, which may not be fully representative for the 3-D volumes in which the backscatter measurements were performed. For example, pores detected in the SAM image may not have been oriented perpendicular to the imaging plane, which would lead to an overestimation of the pore diameter in the 2-D-image and a different backscatter characteristic. Pores may extend axially over a portion of bone shorter than the axial extension (along the y-axis) probed by the CortBS scan. Likewise, pores probed by CortBS may not intersect the SAM image plane. These effects would alter both amplitude and shape of the pore size distribution and the resulting modeled backscatter coefficient; 2) SAM had limited resolution and pixel size (12 μm $\times$ 12 μm), for which particularly the estimation of small pore diameters may be prone to digitization errors; 3) pores are not always cylindrical in shape; 4) the model backscatter cross section was derived using invariable tissue properties, but the measured acoustic impedance exhibits considerable intrasample variability; and 5) the variability in the pore size distribution was small in the evaluated samples.

Therefore, we have chosen to use multivariate regression to predict the structure and material properties measured by SAM based on all backscatter parameters. As expected, cortical thickness was not associated with any backscatter parameter, indicating that the endosteal bone interface reflection had been effectively removed from the analysis, even in samples with thickness values < 3 mm. The acoustic impedance was associated with the periosteal surface reflection amplitude (I_{ref}), the mean cortical pore backscatter coefficient, and the frequency dependence of the attenuation α_f. Whereas it is obvious that the acoustic impedance mismatch between tissue matrix and water inside the pores and outside the bone affects the amplitudes of reflected and scattered waves, the association with α_f suggests that the impedance had an effect on the scattering properties. This hypothesis was further supported by the impact of α_f on most parameters describing the pore diameter distribution ($\text{Ct.Po.Dm}^{\text{peak}}$, Ct.Po.Dm^{Q90}, and $\text{rel.Po.n}_{100\ \mu\text{m}}$). Thus, α_f can be seen as a tuning parameter that compensates for the violation of the assumption of invariant tissue impedance in the backscatter model. Likewise, the mean backscatter amplitude and the model *Offset* parameter were required in addition to Ct.Po.Dm distribution parameters to predict porosity and pore density using the backscatter model. An important advantage of the model-based parameter estimation is that nonlinear features of the backscatter coefficient are parameterized into a set of variables. By different combinations of these parameters, different structural and material properties in the same bone, and even the aBMD at a different measurement region could be predicted independently. Ct.Po has been predicted with an accuracy of 1.95 %, which is slightly better than the accuracy of 2.2% measured in the same set of bones using bidirectional axial transmission [15] and similar (in terms of R^2) with a pulse-echo method backscatter method proposed by Eneh *et al.* [48]. To the best of our knowledge, this is the first nonionizing method that can assess independently and noninvasively tissue impedance, pore density, and characteristic features of the pore size distribution. The prevalence of large cortical pores and cortical thinning in the tibia has been shown to reflect a compromised femoral neck structure and reduced femur strength [1], [37]. Except for the ultimate force under sideway fall conditions, the prediction accuracy of the mechanical properties of the proximal femur was better using Ct.Th and backscatter parameters than that of aBMD.

B. Limitations

This study has several limitations. There was a limited sample size. A total number of 19 left tibia shaft samples were used in this study. One SAM image could not be used for analysis, and the other samples were obtained from rather old donors. Therefore, the range of structural variations in the evaluated bones did not resemble the structure typically found in young, healthy individuals. The theoretical model assumed the composition of scattering from circular pores in a homogenous tissue matrix. As can be seen in the SAM image (Fig. 1), the tissue matrix is not heterogenous, pores were not circular in shape, and the orientation of the long axis of the cylindrical pores is not always parallel to the bone's long axis. Whereas incorporating tissue heterogeneity did not have a significant impact on the sound propagation velocity through the femoral neck [32], it may have an impact on the spectral backscatter characteristics. In particular, the increasing pore size from the periosteal to the endosteal interfaces will eventually result in a gradual change of the effective sound propagation velocity [49], which has not been considered in the current estimations of backscatter and attenuation coefficients. The pore diameter was calculated using the equivalent diameter, corresponding to the diameter of a circle with the same area. Moreover, there was a nonnegligible mismatch between the SAM and ultrasound measurement positions in two samples. This may have affected the multivariate model accuracy. Finally, the combination of strong reflection amplitude from the periosteal bone surface, weak scattering from cortical pores, and strong attenuation inside the cortical bone tissue requires a high-dynamic range. Finally, our data have been captured with 10-bit resolution and a corresponding dynamic range of approximately 25-dB *ex vivo*. Despite these limitations, this study validates that the backscatter parameters can be used to predict cortical bone microstructural and material properties.

C. Transition to Future in Vivo Measurements

This study has been performed using a clinical ultrasound scanner. Therefore, the transition to *in vivo* measurements is straightforward. Major advantages of the method compared with other quantitative cortical bone measurement techniques,

such as axial transmission [3] and single-element pulse-echo ultrasound [48], are that it provides image guidance and that the analyzed signals originate from the pores and not from reflections at periosteal and endosteal bone interfaces. Moreover, the multidirectional volume scan combined with the developed data processing algorithms provides optimal control of the beam inclination relative to the bone surface. Therefore, positioning artifacts during data acquisition and analysis can be effectively avoided. Soft tissue has a strong impact on axial transmission measurements and limits its application to individuals with relatively low body mass index [3]. Although the effect of soft tissue has not been investigated in this study, we anticipate no compromising impact on the structure parameter estimations, as all spectra are normalized to the spectrum of the surface reflection. However, the prediction of the acoustic impedance may not be possible or at least less accurate *in vivo*, and as for this prediction model, the surface reflection amplitude I_{Ref} has been used.

The spectral analysis of 128-channel data required a dedicated acquisition hardware attached to the system. Similar scanner systems are nowadays widely available. We anticipate that the evaluation of the pore diameter distribution has the potential to establish novel biomarkers that are sensitive to discriminate pathological tissue remodeling from normal age and gender-specific alterations prior to the reduction of bone strength. The latter is predominantly predicted by the reduction of cortical thickness [37], which can be measured with the same system [44] or similar multichannel systems [4] in combination with the compressional sound velocity by means of refraction corrected imaging, or alternatively by means of axial transmission ultrasound [3], [15]. Thus, the combined assessment of cortical thickness, sound velocity, and pore size distribution in a mobile, nonionizing measurement system could have a major impact on preventing osteoporotic fractures.

V. Conclusion

This article presents a cortical bone backscatter model, which was used to predict cortical bone structural and material properties in human tibia bones *ex vivo*. The results have demonstrated that Ct.Po, pore density, and the cortical pore size distribution can be predicted from the backscatter and attenuation coefficients and that the structural properties in combination with cortical thickness are predictive for mechanical properties of the proximal femur. This backscatter model suggests that the frequency range from 4 to 10 MHz is suitable to assess normal age-related changes of the pore microstructure noninvasively and to distinguish them from pathologically increased pore sizes during the onset of osteoporosis.

VI. Conflicts of Interest

Dr. G. Iori, Dr. J. Du, and Dr. K. Raum have the patent "CortBS: Ultrasonic method for determining pore dimensions in cortical bone" pending.

References

[1] G. Iori *et al.*, "Large cortical bone pores in the tibia are associated with proximal femur strength," *PLoS ONE*, vol. 14, no. 4, Apr. 2019, Art. no. e0215405.

[2] K. Chiba *et al.*, "Precision of second-generation high-resolution peripheral quantitative computed tomography: Intra- and intertester reproducibilities and factors involved in the reproducibility of cortical porosity," *J. Clin. Densitometry*, vol. 21, no. 2, pp. 295–302, Apr. 2018.

[3] J. Schneider *et al.*, "*In vivo* measurements of cortical thickness and porosity at the proximal third of the tibia using guided waves: Comparison with site-matched peripheral quantitative computed tomography and distal high-resolution peripheral quantitative computed tomography," *Ultrasound Med. Biol.*, vol. 45, no. 5, pp. 1234–1242, May 2019.

[4] G. Renaud, P. Kruizinga, D. Cassereau, and P. Laugier, "*In vivo* ultrasound imaging of the bone cortex," *Phys. Med. Biol.*, vol. 63, no. 12, Jun. 2018, Art. no. 125010.

[5] N. E. Lassen *et al.*, "Coupling of bone resorption and formation in real time: New knowledge gained from human haversian BMUs," *J. Bone Mineral Res.*, vol. 32, no. 7, pp. 1395–1405, Jul. 2017.

[6] C. D. Thomas, S. A. Feik, and J. G. Clement, "Increase in pore area, and not pore density, is the main determinant in the development of porosity in human cortical bone," *J. Anatomy*, vol. 209, no. 2, pp. 219–230, 2006.

[7] H. M. Macdonald, K. K. Nishiyama, J. Kang, D. A. Hanley, and S. K. Boyd, "Age-related patterns of trabecular and cortical bone loss differ between sexes and skeletal sites: A population-based HR-pQCT study," *J. Bone Mineral Res.*, vol. 26, no. 1, pp. 50–62, Jan. 2011.

[8] H. Chen, X. Zhou, S. Shoumura, S. Emura, and Y. Bunai, "Age- and gender-dependent changes in three-dimensional microstructure of cortical and trabecular bone at the human femoral neck," *Osteoporosis Int.*, vol. 21, no. 4, pp. 627–636, 2010.

[9] J. M. Patsch *et al.*, "Increased cortical porosity in type 2 diabetic postmenopausal women with fragility fractures," *J. Bone Minerals Res.*, vol. 28, no. 2, pp. 313–324, 2013.

[10] Y. Bala, R. Zebaze, A. Ghasem-Zadeh, E. J. Atkinson, S. Iuliano, J. M. Peterson, S. Amin, A. Bjornerem, L. J. Melton, H. Johansson, J. A. Kanis, S. Khosla, and E. Seeman, "Cortical porosity identifies women with osteopenia at increased risk for forearm fractures," *J. Bone Mineral Res.*, vol. 29, no. 6, pp. 1356–1362, 2014.

[11] D. M. Cooper, C. E. Kawalilak, K. Harrison, B. D. Johnston, and J. D. Johnston, "Cortical bone porosity: What is it, Why is it important, and how can we detect it?" *Current Osteoporosis Rep.*, vol. 14, no. 5, pp. 187–198, 2016.

[12] R. Zebaze and E. Seeman, "Cortical bone: A challenging geography," *J. Bone Minerals Res.*, vol. 30, no. 1, pp. 24–29, 2015.

[13] C. S. Rajapakse, M. Bashoor-Zadeh, C. Li, W. Sun, A. C. Wright, and F. W. Wehrli, "Volumetric cortical bone porosity assessment with MR imaging: Validation and clinical feasibility," *Radiology*, vol. 276, no. 2, pp. 526–535, 2015.

[14] J.-G. Minonzio *et al.*, "Bone cortical thickness and porosity assessment using ultrasound guided waves: An *ex vivo* validation study," *Bone*, vol. 116, pp. 111–119, Nov. 2018.

[15] J. Schneider *et al.*, "*Ex vivo* cortical porosity and thickness predictions at the tibia using full-spectrum ultrasonic guided-wave analysis," *Arch. Osteoporosis*, vol. 14, no. 1, p. 21, Dec. 2019.

[16] N. J. Wachter *et al.*, "Correlation of bone mineral density with strength and microstructural parameters of cortical bone *in vitro*," *Bone*, vol. 31, no. 1, pp. 90–95, 2002.

[17] C. M. Andreasen, J.-M. Delaisse, B. C. van der Eerden, J. P. van Leeuwen, M. Ding, and T. L. Andersen, "Understanding age-induced cortical porosity in women: The accumulation and coalescence of eroded cavities upon existing intracortical canals is the main contributor," *J. Bone Mineral Res.*, vol. 33, no. 4, pp. 606–620, Apr. 2018.

[18] H. M. Britz, C. D. L. Thomas, J. G. Clement, and D. M. L. Cooper, "The relation of femoral osteon geometry to age, sex, height and weight," *Bone*, vol. 45, no. 1, pp. 77–83, Jul. 2009.

[19] K. L. Bell, N. Loveridge, J. Power, N. Garrahan, B. F. Meggitt, and J. Reeve, "Regional differences in cortical porosity in the fractured femoral neck," *Bone*, vol. 24, no. 1, pp. 57–64, Jan. 1999.

[20] C. M. Andreasen *et al.*, "The generation of enlarged eroded pores upon existing intracortical canals is a major contributor to endocortical trabecularization," *Bone*, vol. 130, Jan. 2020, Art. no. 115127.

[21] M. F. Santarelli and L. Landini, "A model of ultrasound backscatter for the assessment of myocardial tissue structure and architecture," *IEEE Trans. Biomed. Eng.*, vol. 43, no. 9, pp. 901–911, Sep. 1996.

[22] Y. W. Yuan and K. K. Shung, "Ultrasonic backscatter from flowing whole blood. I: Dependence on shear rate and hematocrit," *J. Acoust. Soc. Amer.*, vol. 84, no. 1, pp. 52–58, 1988.

[23] J. Mamou and M. L. Oelze, *Quantitative Ultrasound in Soft Tissues*. Dordrecht, The Netherlands: Springer, 2013.
[24] J. Mamou, M. L. Oelze, W. D. O'Brien, and J. F. Zachary, "Identifying ultrasonic scattering sites from three-dimensional impedance maps," *J. Acoust. Soc. Amer.*, vol. 117, no. 1, pp. 413–423, 2005.
[25] J. J. Faran, "Sound scattering by solid cylinders and spheres," *J. Acoust. Soc. Amer.*, vol. 23, no. 4, pp. 405–418, Jul. 1951.
[26] H. Hosseini and N. Namazi, "Acoustic scattering of spherical waves incident on a long fluid-saturated poroelastic cylinder," *Acta Mechanica*, vol. 223, no. 10, pp. 2075–2089, Oct. 2012.
[27] F. Jenson, F. Padilla, and P. Laugier, "Prediction of frequency-dependent ultrasonic backscatter in cancellous bone using statistical weak scattering model," *Ultrasound Med Biol*, vol. 29, no. 3, pp. 455–464, 2003.
[28] F. Padilla, F. Peyrin, and P. Laugier, "Prediction of backscatter coefficient in trabecular bones using a numerical model of three-dimensional microstructure," *J. Acoust. Soc. Amer.*, vol. 113, no. 2, pp. 1122–1129, 2003.
[29] K. A. Wear, F. Padilla, and P. Laugier, "Comparison of the Faran cylinder model and the weak scattering model for predicting the frequency dependence of backscatter from human cancellous femur *in vitro*," *J. Acoust. Soc. Amer.*, vol. 124, no. 3, pp. 1408–1410, 2008.
[30] Y. Karbalaeisadegh, O. Yousefian, G. Iori, K. Raum, and M. Müller, "Acoustic diffusion constant of cortical bone: Numerical simulation study of the effect of pore size and pore density on multiple scattering," *J. Acoust. Soc. Amer.*, vol. 146, no. 2, p. 1015, 2019.
[31] J. Minonzio *et al.*, "Ultrasound-based estimates of cortical bone thickness and porosity are associated with nontraumatic fractures in postmenopausal women: A pilot study," *J. Bone Mineral Res.*, vol. 34, no. 9, pp. 1585–1596, Sep. 2019.
[32] Q. Grimal *et al.*, "Modeling of femoral neck cortical bone for the numerical simulation of ultrasound propagation," *Ultrasound Med. Biol.*, vol. 40, no. 5, pp. 1015–1026, 2014.
[33] V. T. Potsika *et al.*, "Computational study of the effect of cortical porosity on ultrasound wave propagation in healthy and osteoporotic long bones," *Materials*, vol. 9, no. 3, p. 205, Mar. 2016.
[34] M. Saeki *et al.*, "FDTD simulation study of ultrasonic wave propagation in human radius model generated from 3D HR-pQCT images," *Phys. Med.*, vol. 10, Dec. 2020, Art. no. 100029.
[35] G. Iori *et al.*, "BMD-based assessment of local porosity in human femoral cortical bone," *Bone*, vol. 114, pp. 50–61, Sep. 2018.
[36] O. T. von Ramm and S. W. Smith, "Beam steering with linear arrays," *IEEE Trans. Biomed. Eng.*, vol. BME-30, no. 8, pp. 438–452, Aug. 1983.
[37] G. Iori *et al.*, "Cortical thinning and accumulation of large cortical pores in the tibia reflect local structural deterioration of the femoral neck," *Bone*, vol. 137, Aug. 2020, Art. no. 115446.
[38] S. Lakshmanan, A. Bodi, and K. Raum, "Assessment of anisotropic tissue elasticity of cortical bone from high-resolution, angular acoustic measurements," *IEEE Trans. Ultrason., Ferroelectr., Freq. Control*, vol. 54, no. 8, pp. 1560–1570, Aug. 2007.
[39] A. V. Belikov, "The number of key carcinogenic events can be predicted from cancer incidence," *Sci. Rep.*, vol. 7, no. 1, p. 12170, Dec. 2017.
[40] M. L. Oelze and J. F. Zachary, "Examination of cancer in mouse models using high-frequency quantitative ultrasound," *Ultrasound Med. Biol.*, vol. 32, no. 11, pp. 1639–1648, 2006.
[41] K. A. Wear, "Frequency dependence of ultrasonic backscatter from human trabecular bone: Theory and experiment," *J. Acoust. Soc. Amer.*, vol. 106, no. 6, pp. 3659–3664, 1999.
[42] E. Bossy, M. Talmant, and P. Laugier, "Three-dimensional simulations of ultrasonic axial transmission velocity measurement on cortical bone models," *J. Acoust. Soc. Amer.*, vol. 115, no. 5, pp. 2314–2324, 2004.
[43] K. Rohde *et al.*, "Influence of porosity, pore size, and cortical thickness on the propagation of ultrasonic waves guided through the femoral neck cortex: A simulation study," *IEEE Trans. Ultrason., Ferroelectr., Freq. Control*, vol. 61, no. 2, pp. 302–313, Feb. 2014.
[44] H. Nguyen Minh, J. Du, and K. Raum, "Estimation of thickness and speed of sound in cortical bone using multifocus pulse-echo ultrasound," *IEEE Trans. Ultrason., Ferroelectr., Freq. Control*, vol. 67, no. 3, pp. 568–579, Mar. 2020.
[45] M. F. Insana, R. F. Wagner, D. G. Brown, and T. J. Hall, "Describing small-scale structure in random media using pulse-echo ultrasound," *J. Acoust. Soc. Amer.*, vol. 87, no. 1, pp. 179–192, Jan. 1990.
[46] M. Sasso, G. Haiat, Y. Yamato, S. Naili, and M. Matsukawa, "Frequency dependence of ultrasonic attenuation in bovine cortical bone: An *in vitro* study," *Ultrasound Med. Biol.*, vol. 33, no. 12, pp. 1933–1942, 2007.
[47] M. Sasso, G. Haïat, Y. Yamato, S. Naili, and M. Matsukawa, "Dependence of ultrasonic attenuation on bone mass and microstructure in bovine cortical bone," *J. Biomechanics*, vol. 41, no. 2, pp. 347–355, Jan. 2008.
[48] C. T. Eneh, I. O. Afara, M. K. Malo, J. S. Jurvelin, and J. Toyras, "Porosity predicted from ultrasound backscatter using multivariate analysis can improve accuracy of cortical bone thickness assessment," *J. Acoust. Soc. Amer.*, vol. 141, no. 1, p. 575, 2017.
[49] K. Takano, Y. Nagatani, and M. Matsukawa, "Simulation study of axial ultrasound transmission in heterogeneous cortical bone model," *Jpn. J. Appl. Phys.*, vol. 56, no. 7, Jul. 2017, Art. no. 07JF29.

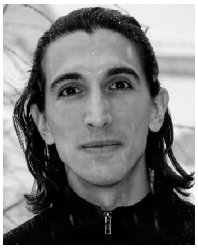

Gianluca Iori (Member, IEEE) was born in Reggio Emilia, Italy, in 1987. He received the M.Sc. degree in mechanical engineering from the Alma Mater Studiorum, University of Bologna, Italy, in 2013, the Degree from the Berlin-Brandenburg School for Regenerative Therapies, Berlin, Germany, in 2019, and the Ph.D. (Dr.-Ing.) degree from the faculty of process sciences of the Berlin Institute of Technology, Berlin, in 2019.

From 2013 to 2014, he was a Research Fellow with the Medical Technology Laboratory, Rizzoli Orthopedic Institute, Bologna, Italy. Since 2020, he has been appointed as a Beamline Scientist with the Synchrotron-Light for Experimental Science and Applications in the Middle East, Allan, Jordan, where he is currently coordinating the design and installation of a synchrotron beamline for X-ray tomography within the European Horizon 2020 project BEATS. His work focuses on imaging and on the mechanics of nature's materials.

Dr. Iori is a member of the Acoustical Society of America, the European Society of Biomechanics, and the Bone Ultrasound Society.

Juan Du was born in Hebei, China, in 1987. She received the B.Sc. degree in control, detection, and navigation from Beihang University, Beijing, China, in 2009, and the M.Sc. and Ph.D. degrees in electrical engineering from the University of Minnesota at Twin Cities, Minneapolis, MN, USA, in 2012 and 2016, respectively.

From 2014 to 2015, she was with the Department of Research and Development, Medtronic, Inc., Minneapolis, MN, USA, developing algorithms for ECG signal processing, the graphic user interface for physicians, and performing ultrasound acoustic field simulation and transducer modeling and optimization, which resulted in four granted U.S. patents. From 2016 to 2018, she was a Postdoctoral Researcher with the Berlin-Brandenburg School for Regenerative Therapies, Charité—Universitätsmedizin Berlin, Berlin, Germany. She is currently with Digital Endoscopy GmbH, Friedberg, Germany. Her research interests include ultrasound microvascular imaging, ultrasound acoustics, biomedical-related signal and image processing, DSP design and implementation, and medical device development.

Janos Hackenbeck received the B.Sc. degree in physics from Freie Universität Berlin, Berlin, Germany, in 2012, the M.Eng. degree in physical engineering/medical physics from the Beuth University of Applied Sciences, Berlin, in 2016.

From 2015 to 2017, he was doing research in the development of ultrasound diagnosis on musculoskeletal diseases with the Berlin-Brandenburg School for Regenerative Therapies, Charité—Universitätsmedizin Berlin, Berlin. He is currently working in the industry as a Software Engineer on digital operating-room integration and medical product certification.

Vantte Kilappa received the master's and Ph.D. degrees in physics from Jyväskylä University, Jyväskylä, Finland, in 2008 and 2014, respectively.

He joined as a Postdoctoral Researcher with Prof. Raum's research group at Charité—Universitätsmedizin Berlin, Berlin, from 2015 to 2016. During this time, he worked on the development of the measurement and analysis software and protocols for the ultrasound cortical backscatter measurements. He received a postdoctoral researcher grant from the Finnish Cultural Foundation in 2015. His research interests were mainly focused on signal and image processing and ultrasound acoustics. He is currently working in the technology industry as a Senior Software Engineer and a Consultant with Mango Solutions Oy, Puuppola, Finland. He is building cloud solutions for distributed measurement systems.

Kay Raum (Member, IEEE) was born in Halle, Germany, in 1972. He received the Diploma and Ph.D. (Dr.rer.nat.) degrees in physics from Martin-Luther-University Halle-Wittenberg, Halle, in 1997 and 2002, respectively.

He was a Visiting Scholar with Bioacoustics Research Laboratory, University of Illinois at Urbana–Champaign, Champaign, IL, USA, from 1995 to 1996. From 1997 to 2003, he was a Research Assistant with Medical Faculty, Martin-Luther-University Halle-Wittenberg. In 2004, he was a Post-Doctoral Fellow with the French National Center of Scientific Research, Paris, France, and joined the Laboratoire d'Imagerie Paramétrique, Sorbonne University Pierre and Marie Curie Campus, Paris. In 2006, he became the Research Head of the Medical Department, Interdisciplinary Center for Musculoskeletal Diseases, Martin Luther University. In 2009, he was appointed as a Full Professor for engineering basis of regeneration with the Berlin-Brandenburg School for Regenerative Therapies, Charité—Universitätsmedizin Berlin, Berlin, Germany. He has authored over 75 original articles and several book chapters. His research interests include the development and applications of ultrasound and X-ray tomography in musculoskeletal research, diagnosis, and therapy.

Dr. Raum is a Founding Member and a Treasurer of the International Bone Ultrasound Society and a member of the Acoustical Society of America, the Bone Ultrasound Society, the German Society for Biomedical Technology (VDE-DGBMT), and the German Osteology Society. He is an Associate Editor of the journals *Ultrasound in Medicine and Biology* and *Ultrasonic Imaging*.